Wavefield tomography using RTM backscattering

Esteban Díaz and Paul Sava, Center for Wave Phenomena, Colorado School of Mines*

SUMMARY

Reverse time migration (RTM) backscattering contains kinematic information that can be used to constrain velocity models. The backscattering results from the correlation between forward and back propagated wavefields originating at sharp interfaces, e.g. sediment-salt interfaces. The synchronization between these wavefields depends on the sediment velocity section and on the correct interpretation of the sharp boundary. Therefore, we can use backscattering events along with reflection and diving waves to define a joint optimization problem for velocity model building. The gradient required for model optimization suffers from cross-talk, similar to the more conventional RTM images. In order to avoid the cross-talk, we use a directional filter based on Poynting vectors which preserves the components of the wavefield traveling in the same direction. Using backscattered waves for constraining the velocity in the sediment section requires defining the top of salt in advance, which implies a dynamic workflow for model building in salt environments where both sediment velocity and salt interface change iteratively during inversion.

INTRODUCTION

In complex models with sharp boundaries, the use of the two-way wave equation produces low wavenumber events in the image which are normally regarded as artifacts. These events exist due to the correlation of waves which are not accounted for in the cross-correlation imaging condition (Claerbout, 1985). Several filtering approaches have been proposed to eliminate such events from the image. We could classify such methods as either pre-imaging filtering (Fletcher et al., 2005; Yoon et al., 2004; Liu et al., 2011) or post-imaging filtering (Youn and Zhou, 2001; Guitton et al., 2007; Zhang and Sum, 2009; Kaelin and Carvajal, 2011).

Although RTM backscattering events are noise for imaging purposes, they carry kinematic information (Díaz and Sava, 2012). The low-wavenumber events are due to the correlation of waves traveling in the same direction; therefore, if the velocity model is correct, then the wavefields are in optimal synchronization. For reflected data, the synchronization occurs at the reflector position if the velocity is correct. Since both reflected and transmitted wavefields share the same kinematic behavior, we can design a joint optimization problem that improves the synchronization of all the data simultaneously, thus allowing us to refine the model and use the RTM backscattering as a source of information instead of treating it as noise.

To optimize the velocity model, we set up an inversion in the image domain (Sava and Biondi, 2004; Fliedner and Bevc, 2008; Shen and Symes, 2008; Yang and Sava, 2011). The image domain approach seeks the kinematic synchronization of the wavefields at an image location. Therefore, the aim of this method is to improve the image focusing rather than to match the dynamic information of the wavefields, as is done in the data-domain approach. This increases the robustness of the method but limits its ability to construct high resolution models. One way to formulate the problem in the image space is by using extended images (Rickett and Sava, 2002; Sava and Fomel, 2006; Sava and Vasconcelos, 2011), from which we can extract wavefield similarities in space and time (Shen et al., 2003; Yang and Sava, 2010). Although extended images are normally used for optimizing the reflected data information, Díaz and Sava (2012) show that the RTM backscattered energy also maps to zero time-lag and space-lag when the velocity model is correct.

In this paper, we demonstrate that it is possible to use the backscattered and diving waves for image-domain wavefield tomography. Using the two-way wave equation operator allows simultaneous inversion based on the reflected, diving, and backscattered waves. We formulate the tomography problem using the adjoint state method (ASM), which is an efficient technique for gradient-based optimization (Plessix, 2006). However, the gradient computed using the ASM suffers from cross-talk between forward and backscattered waves, which produces undesirable reflector-like events. In order to avoid the unwanted correlations, we apply a directional filter designed to keep the contributions between wavefields traveling in the same direction during the correlation step of the gradient computation. This filter is based on the Poynting vectors of the extrapolated wavefields (Yoon et al., 2004), although other filtering techniques can be used instead.

RTM BACKSCATTERING

RTM backscattering is produced in the presence of sharp models, e.g. sediment-salt interfaces. In such cases, wavefields extrapolated with a two-way operator, e.g. the scalar wave equation

$$\frac{1}{v^2(\mathbf{x})}\frac{\partial^2 u(\mathbf{x},t)}{\partial t^2} - \nabla^2 u(\mathbf{x},t) = f(\mathbf{x},t) \qquad (1)$$

contain forward and backscattered components. Here, $u(\mathbf{x},t)$ is the reconstructed wavefield, $v(\mathbf{x})$ is the medium velocity and $f(\mathbf{x},t)$ is the source function. Therefore, we can write the source wavefield as a superposition of two components:

$$u_s(\mathbf{x},t) = u_s^b(\mathbf{x},t) + u_s^f(\mathbf{x},t), \qquad (2)$$

where the superscripts ^{b} and ^{f} correspond to the backscattered and forward scattered wavefields from the sharp boundary, respectively. Similarly, for the receiver wavefield,

$$u_r(\mathbf{x},t) = u_r^b(\mathbf{x},t) + u_r^f(\mathbf{x},t). \tag{3}$$

Using such wavefields (equations 2 and 3) in the conventional imaging condition (Claerbout, 1985)

$$R(\mathbf{x}) = \sum_e \sum_t u_s(e,\mathbf{x},t) u_r(e,\mathbf{x},t), \tag{4}$$

produces four different image combinations:

$$R(\mathbf{x}) = R^{ff}(\mathbf{x}) + R^{bb}(\mathbf{x}) + R^{bf}(\mathbf{x}) + R^{fb}(\mathbf{x}). \tag{5}$$

Two images, $R^{ff}(\mathbf{x})$ and $R^{bb}(\mathbf{x})$, represent the earth reflectivity, and the other two combinations, $R^{bf}(\mathbf{x})$ and $R^{fb}(\mathbf{x})$, represent backscattering.

The different wavefield combinations can also be analyzed in the extended image space (Rickett and Sava, 2002; Sava and Fomel, 2006; Sava and Vasconcelos, 2011). The extended imaging condition (EIC) is defined as

$$R(\mathbf{x},\boldsymbol{\lambda},\tau) = \sum_e \sum_t u_s(e,\mathbf{x}-\boldsymbol{\lambda},t-\tau) u_r(e,\mathbf{x}+\boldsymbol{\lambda},t+\tau). \tag{6}$$

Here $\boldsymbol{\lambda}$ and τ represent space and time correlation lags, respectively. The extended images provide information about the consistency between source and receiver wavefields. RTM backscattering produces four different combinations for the extended image:

$$\begin{aligned} R(\mathbf{x},\boldsymbol{\lambda},\tau) = {} & R^{ff}(\mathbf{x},\boldsymbol{\lambda},\tau) + R^{bb}(\mathbf{x},\boldsymbol{\lambda},\tau) \\ & + R^{bf}(\mathbf{x},\boldsymbol{\lambda},\tau) + R^{fb}(\mathbf{x},\boldsymbol{\lambda},\tau), \end{aligned} \tag{7}$$

which is similar to the ones seen in the conventional image.

In the conventional image $R(\mathbf{x})$, both backscattered and reflected energy coexist above sharp interfaces, for example, due to the presence of a salt body. The two components are usually separated based on the spectral content (the artifacts have low wavenumber content, whereas the reflectivity has high wavenumber content). This separation is normally done using some sort of high-pass filter, like a Laplacian operator (Youn and Zhou, 2001; Zhang and Sum, 2009) or by least-squares filtering (Guitton et al., 2007). The separation is not perfect in areas with similar spectral content. In the extended image space, however, the reflected and backscattered energy have unique mapping patterns (Díaz and Sava, 2012), which can be used to separate both components (Kaelin and Carvajal, 2011).

Figures 1(a)-1(c) show the space-lag gather dependency with respect to the velocity error. These space-lag gathers are generated after stacking the contribution from different experiments. The backscattering maps vertically in the gathers, spreads away from zero lag with the velocity error, and thus emulates the defocusing of the reflected data. The backscattering above the interface is the expression of the defocusing at the sharp boundary. Since both reflected and backscattered data share similar velocity dependency, we can design an inverse problem that optimizes both type of events simultaneously, as suggested by Díaz and Sava (2012).

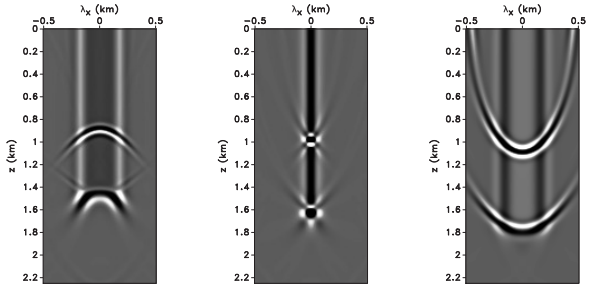

Figure 1: Space-lag gathers for (a) low, (b) correct, and (c) high velocity. The data is generated in a model with two reflectors, with the deepest one coming from a sharp velocity contrast.

WAVEFIELD TOMOGRAPHY

In order to analyze the velocity model error, we can make use of the semblance principle which seeks image consistency as a function of extended image parameters. Stork (1992) implements the idea using the consistency between common offset images. Symes and Carazzone (1991) exploit this concept using the differential semblance optimization (DSO) method. DSO can also be used to increase the flatness of angle gathers or focusing in space-lag gathers. Shen and Symes (2008) and Yang and Sava (2011) use the consistency criterion in extended images to formulate a tomographic problem based on space-lag gathers or joint space-lag and time-lag gathers, respectively.

If the velocity is correct, the space-lag gathers (Rickett and Sava, 2002) show maximum focusing at $\boldsymbol{\lambda} = 0$. This observation derives from the fact that the source and receiver wavefields are synchronized at the reflector position. The velocity model can be improved by minimizing the energy outside zero space lag, which translates into minimizing the objective function (Shen and Symes, 2008):

$$J = \frac{1}{2} \left|\left| P(\boldsymbol{\lambda}) R(\mathbf{x},\boldsymbol{\lambda}) \right|\right|^2, \tag{8}$$

where $P(\boldsymbol{\lambda}) = |\boldsymbol{\lambda}|$ is an operator that penalizes the energy outside $\boldsymbol{\lambda} = 0$. Following the notation in Yang and Sava (2011), we can express $R(\mathbf{x},\boldsymbol{\lambda})$ as

$$R(\mathbf{x},\boldsymbol{\lambda}) = \sum_e \sum_{\boldsymbol{\lambda}} T(-\boldsymbol{\lambda}) u_s(e,\mathbf{x},t) T(+\boldsymbol{\lambda}) u_r(e,\mathbf{x},t), \tag{9}$$

where $T(\pm\boldsymbol{\lambda})$ is a space-shift operator applied to the source or receiver wavefields.

We compute the gradient of equation 8 using the Adjoint State Method (ASM) (Tarantola, 1984; Plessix, 2006).

The adjoint source with respect to the source wavefield is

$$g_s(\mathbf{x},e) = \sum_{\boldsymbol{\lambda}} T(-\boldsymbol{\lambda})P^2(\boldsymbol{\lambda})R(\mathbf{x},\boldsymbol{\lambda})T(-\boldsymbol{\lambda})u_r(e,\mathbf{x},t), \tag{10}$$

and the adjoint source with respect to the receiver wavefield is

$$g_r(\mathbf{x},e) = \sum_{\boldsymbol{\lambda}} T(+\boldsymbol{\lambda})P^2(\boldsymbol{\lambda})R(\mathbf{x},\boldsymbol{\lambda})T(-\boldsymbol{\lambda})u_s(e,\mathbf{x},t). \tag{11}$$

We construct the adjoint state variables by injecting the adjoint sources at the gather positions and by extrapolating the wavefields using the adjoint modeling operators. The adjoint source wavefield $a_s(e,\mathbf{x},t)$ is reconstructed backward in time, whereas the adjoint receiver wavefield $a_r(e,\mathbf{x},t)$ is reconstructed forward in time. During the gradient computation, we expect to correlate state and adjoint state wavefields traveling in the same direction. However, if backscattering is present in the wavefield, we obtain cross-talk similar to that seen in RTM. The cross-talk in this case is generated by the correlation of wavefields traveling in the opposite direction. To attenuate the cross-talk, we use a filter that preserves the wavefield components traveling in the same direction. We can find the direction of propagation using the approach of Yoon et al. (2004), which constructs the Poynting vectors $\mathbf{P}(e,\mathbf{x},t)$ using the equation

$$\mathbf{P}(e,\mathbf{x},t) \propto \frac{\partial u(e,\mathbf{x},t)}{\partial t}\nabla u(e,\mathbf{x},t), \tag{12}$$

where u can be either the source or the receiver wavefield.

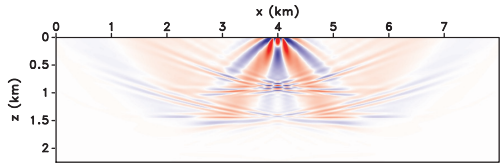

(a)

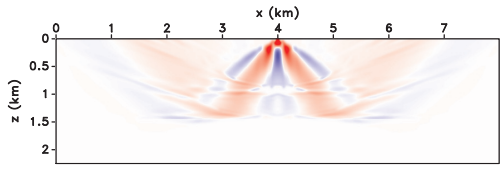

(b)

Figure 2: Gradients obtained for low velocity using space lag gathers (a) without filter and (b) with filter. These gradients are computed with the space-lag gather shown in Figure 1(a).

To preserve just the wavefield components traveling in the same direction, we can compute a weighting function $W(\theta)$ with

$$\theta(e,\mathbf{x},t) = \cos^{-1}\left(\frac{\mathbf{P}_s(e,\mathbf{x},t)\cdot\mathbf{P}_r(e,\mathbf{x},t)}{|\mathbf{P}_s(e,\mathbf{x},t)||\mathbf{P}_r(e,\mathbf{x},t)|}\right) \tag{13}$$

such that we preserve the wavefield cross-correlation for which $\mathbf{P}_s(e,\mathbf{x},t)\cdot\mathbf{P}_r(e,\mathbf{x},t) \approx 1$, i.e. when the direction of propagation is similar within a given tolerance. The weighting function is designed using a cutoff angle a and a Gaussian tapering region σ,

$$W(\theta,a,\sigma) = \begin{cases} 1 : 0^\circ \le \theta < a \\ e^{-(\theta-a)^2/(2\sigma^2)} : a \le \theta \le 180^\circ. \end{cases} \tag{14}$$

This weighting function accepts angles close to zero, and rejects otherwise. Based on this filter, the objective function gradient is

$$\nabla J(\mathbf{x}) = \frac{-2}{v^3(\mathbf{x})}\sum_e\sum_t W(\theta,e)\frac{\partial^2 u_s}{\partial t^2}(e,\mathbf{x},t)a_s(e,\mathbf{x},t) + W(\theta,e)\frac{\partial^2 u_r}{\partial t^2}(e,\mathbf{x},t)a_r(e,\mathbf{x},t), \tag{15}$$

where $\frac{-2}{v^3(\mathbf{x})}\frac{\partial^2}{\partial t^2}$ corresponds to the derivative of the modeling operator (equation 1) with respect to the velocity model. Note that computing a gradient without filtering implies $W(\theta,e) = 1$. This new gradient avoids cross-talk and emphasizes wavefields traveling in the same direction. Figures 2(a) and 2(b) show gradients for low velocity computed using the space-lag gather shown in Figure 1(a) without and with filtering, respectively. The cross-talk is attenuated after filtering.

SALT EXAMPLE

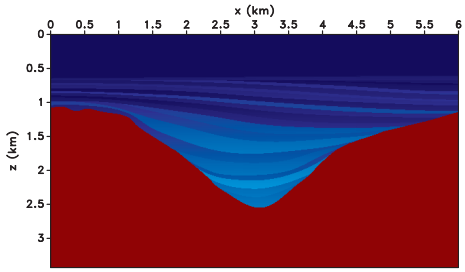

Figure 3: True velocity model considered for the example.

In this section, we illustrate the use of the backscattering and reflected events on a modified version of the Sigsbee 2b model (Paffenholz et al., 2002). We create a new model (Figure 3) based on the small basin formed by the salt intrusion. We simulate data for 61 shots evenly distributed on the surface, with a fixed receiver array at the surface. In order to test our method, we perform a migration with a fast sediment velocity and with a misplaced top of salt, as shown in Figure 4(a).

Figure 5(a) shows the gradient computed using the velocity in Figure 4(a), Figure 5(b) shows the filtered gradient, and Figure 5(c) shows the difference between the gradients in Figures 5(a) and 5(b). One can see that the

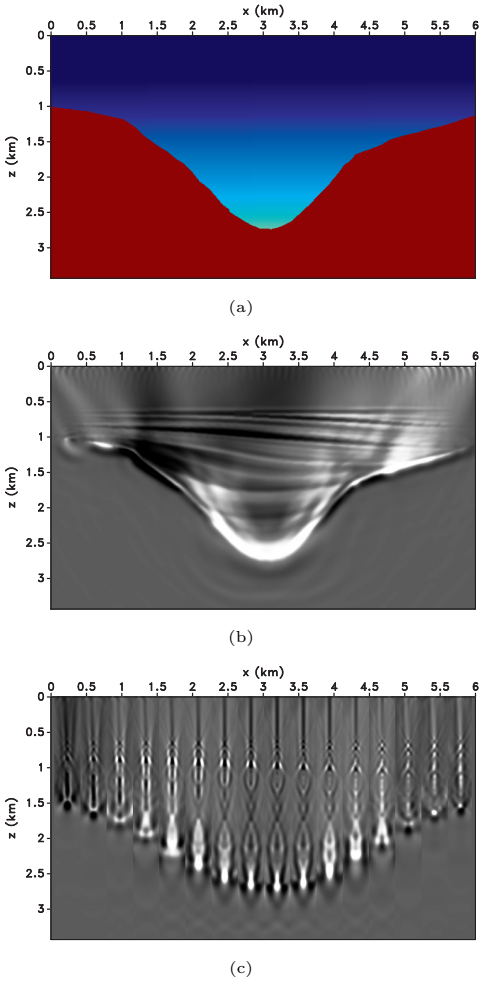

Figure 4: Fast migration velocity (a), RTM image (b), and (c) space-lag gathers evenly distributed in the image.

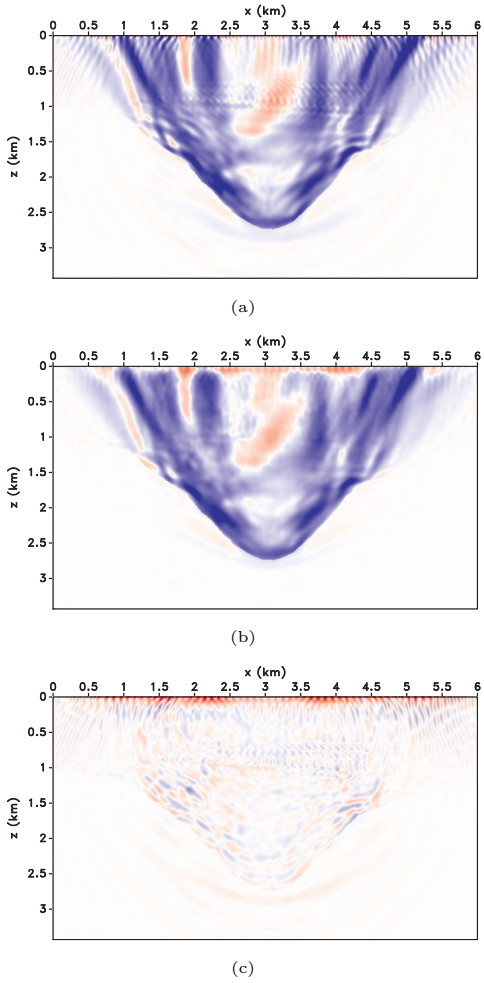

Figure 5: Gradients for salt model example using velocity in Figure 4(a): (a) gradient without filter, (b) gradient with directional filter, and (c) the difference.

gradient energy is concentrated above the sharp boundary; therefore, the update is correctly focused in the sediment basin, and the cross-talk is effectively removed by our filter using Poynting vectors.

Since we use the top of salt for the tomography update, it is necessary to interpret this event at each iteration. Interpretation of salt boundaries could be very difficult and time consuming, especially in complicated salt bodies with overhanging flanks (Ahmed et al., 2012). In this approach, both sediment velocity and top of salt boundary change at each iteration. In practice, one could interpret the salt boundary in the first iteration and look for its changes in the vicinity of the previous solution using, for example, automatic salt interpretation (Lomask et al., 2007; Halpert, 2011).

CONCLUSIONS

We demonstrate that it is possible to use RTM backscattered data in wavefield tomography. The RTM backscattering provides information about the wavefield synchronization and focusing of the sharp boundaries at any place in the image above the boundaries. Sharp models introduce cross-talk in wavefield tomography gradients, which we filter based on propagation directions evaluated with Poynting vectors.

We can use the backscattered information and sharp boundaries in the model to constrain the sediment velocity in the upper section. Using this information requires a dynamic model building workflow, with both the sediment and salt boundaries being updated at every iteration. Although we demonstrate the presence of cross-talk in wavefield tomography with space-lag gathers, this method can also be applied to time-lag and common-image point gathers.

ACKNOWLEDGMENTS

This work was supported by the sponsors of the Center for Wave Phenomena. The numerical examples in this paper use Madagascar open-source software, freely available from http://www.ahay.org. We thank SMAART JV for the Sigsbee synthetic model.

REFERENCES

Ahmed, I., R. Faerber, C. Kumar, and F. Billette, 2012, Interactive velocity model validation (IVMV): SEG Technical Program Expanded Abstracts 2012, 1–5.

Claerbout, J. F., 1985, Imaging the earth's interior: Blackwell Scientific Publications, Inc.

Díaz, E., and P. Sava, 2012, Understanding the reverse time migration backscattering: noise or signal?: SEG Technical Program Expanded Abstracts 2012, 1–6.

Fletcher, R. F., P. Fowler, P. Kitchenside, and U. Albertin, 2005, Suppressing artifacts in prestack reverse time migration: SEG Technical Program Expanded Abstracts, **24**, 2049–2051.

Fliedner, M., and D. Bevc, 2008, Automated velocity model building with wavepath tomography: Geophysics, **73**, VE195–VE204.

Guitton, A., B. Kaelin, and B. Biondi, 2007, Least-squares attenuation of reverse-time-migration artifacts: Geophysics, **72**, S19–S23.

Halpert, A. D., 2011, Model-building with image segmentation and fast image updates: 4035–4039.

Kaelin, B., and C. Carvajal, 2011, Eliminating imaging artifacts in RTM using pre-stack gathers: SEG Technical Program Expanded Abstracts, **30**, 3125–3129.

Liu, F., G. Zhang, S. A. Morton, and J. P. Leveille, 2011, An effective imaging condition for reverse-time migration using wavefield decomposition: Geophysics, **76**, S29–S39.

Lomask, J., R. Clapp, and B. Biondi, 2007, Application of image segmentation to tracking 3d salt boundaries: Geophysics, **72**, P47–P56.

Paffenholz, J., B. McLain, J. Zaske, and P. Keliher, 2002, Subsalt multiple attenuation and imaging: Observations from the Sigsbee 2B synthetic dataset: 72nd Annual International Meeting, SEG, Expanded Abstracts, 2122–2125.

Plessix, R.-E., 2006, A review of the adjoint-state method for computing the gradient of a functional with geophysical applications: Geophysical Journal International, **167**, 495–503.

Rickett, J. E., and P. C. Sava, 2002, Offset and angle-domain common image-point gathers for shot-profile migration: Geophysics, **67**, 883–889.

Sava, P., and B. Biondi, 2004, Wave-equation migration velocity analysis - I: Theory: Geophysical Prospecting, **52**, 593–606.

Sava, P., and S. Fomel, 2006, Time-shift imaging condition in seismic migration: Geophysics, **71**, S209–S217.

Sava, P., and I. Vasconcelos, 2011, Extended imaging conditions for wave-equation migration: Geophysical Prospecting, **59**, 35–55.

Shen, P., and W. W. Symes, 2008, Automatic velocity analysis via shot profile migration: Geophysics, **73**, VE49–VE59.

Shen, P., W. W. Symes, and C. C. Stolk, 2003, Differential semblance velocity analysis by wave-equation migration: SEG Technical Program Expanded Abstracts, **22**, 2132–2135.

Stork, C., 1992, Reflection tomography in the postmigrated domain: Geophysics, **57**, 680–692.

Symes, W., and J. Carazzone, 1991, Velocity inversion by differential semblance optimization: Geophysics, **56**, 654–663.

Tarantola, A., 1984, Inversion of seismic reflection data in the acoustic approximation: Geophysics, **49**, 1259–1266.

Yang, T., and P. Sava, 2010, Moveout analysis of wave-equation extended images: Geophysics, **75**, 151–161.

———, 2011, Image-domain waveform tomography with two-way wave-equation: SEG Technical Program Expanded Abstracts 2011, **508**, 2591–2596.

Yoon, K., K. J. Marfurt, and W. Starr, 2004, Challenges in reversetime migration: SEG Technical Program Expanded Abstracts, 1057–1060.

Youn, O. K., and H. Zhou, 2001, Depth imaging with multiples: Geophysics, **66**, 246–255.

Zhang, Y., and J. Sum, 2009, Practical issues in reverse time migration: true amplitude gathers, noise removal and harmonic source encoding: First Break, **27**, 53–59.